

**A Photogrammetric and Theoretical Analysis of the
CHIME Antenna Feed Positions**

by

Mohamed M. Shaaban

A THESIS SUBMITTED IN PARTIAL FULFILLMENT
OF THE REQUIREMENTS FOR THE DEGREE OF

BACHELOR OF SCIENCE

in

THE FACULTY OF SCIENCE
(Physics and Astronomy)

The University of British Columbia
(Vancouver)

April 2018

© Mohamed M. Shaaban, 2018

Abstract

The Canadian Hydrogen Intensity Mapping Experiment (CHIME) is a transit radio interferometer telescope located at the Dominion Radio Astrophysical Observatory (DRAO) in Penticton, BC, Canada. CHIME aims to probe the accelerating expansion of the universe by mapping the large scale matter distribution in the universe via the 21 cm emission line of neutral hydrogen at red shift $0.8 < z < 2.5$, the era at which Dark Energy began to dominate.

CHIME relies on a regular array of 1024 dual polarized antenna feeds. The focus of this study is to gauge the significance of irregularities in the antenna feed array on the instrument's performance. We use photogrammetry techniques to produce high accuracy measurement of the feed positions relative to each other, thereby determining any irregularities in the antenna array. We then investigate and analyze the basic effects of these irregularities on the instrument's performance with an emphasis on data compression efforts and beam effects.

Table of Contents

Abstract	ii
Table of Contents	iii
List of Tables	v
List of Figures	vi
Glossary	xi
Acknowledgments	xii
1 Introduction	1
1.1 Motivation	1
1.2 Theory & Background	2
1.2.1 Dark Energy & The Expansion of The Universe	2
1.2.2 Baryon Acoustic Oscillation (BAO)	4
1.2.3 Hydrogen Intensity Mapping	5
1.3 Interferometers	7
1.4 An Introduction to CHIME	11
2 Antenna Feed Deviation Measurements	13
2.1 General Method	13
2.2 East-West Deviation	15
2.3 North-South Deviation	21

3 Feed Deviation Effects	27
3.1 Deviation Effects on A Simple Beam Model	27
3.1.1 Simple Beam Model	27
3.1.2 Visibility Phase Effects	30
3.1.3 Visibility Beam Effects	30
3.2 Deviation Effects on Redundant Baseline Stacking	35
4 Discussion & Future Work	37
4.1 Future Work	37
4.2 Conclusion	38
Bibliography	39
A Appendix A	42

List of Tables

Table 1.1	Summary of CHIME instrument salient features	12
-----------	--	----

List of Figures

Figure 1.1	A representation of the evolution of the universe over 13.77 billion years. The x axis represents the progression of time, the vertical extent of the grid depicts the size of the universe. The far left depicts the earliest moments when inflation pushed the quantum fluctuations to cosmological scales. The universe then progressed to the dark ages, epoch of reionization and then galaxies and large structures began to form [23]. CHIME aims to probe the region at which the grid size began to curve outwards indicating acceleration due to dark energy dominance.	6
Figure 1.2	This is a diagram of a two-element interferometer. The two triangles labeled 1 and 2 represent two antenna separated by a baseline vector \vec{b} . The straight orange line represents the wavefront coming from a source in the \hat{s} direction, feeds 1 and 2 are receiving the same signal with a phase offset due to the path difference seen in the diagram (the path to feed 1 is $\vec{b} \cdot \hat{s}$ longer than the path to feed 2) The $\langle \times \rangle$ component of the diagram represents the correlator, the component responsible for combining the signal from the two feeds.	8
Figure 1.3	This diagram shows the same interferometer as Figure 1.2, the orange line represents the spherical wave front upon arrival at the feeds. The parameter Δ parameterizes the deviation from a planar wave and R represents the distance between the wave and the source.	10

Figure 1.4	Photographs of CHIME: The top photograph shows the CHIME telescope from a distance, the four cylindrical reflectors are the large white structures oriented along the north-south direction. At the focal line of each reflector is 256 antenna mounted below a walkway. The bottom photograph shows one of the focal line walkways, the green devices seen in the photograph are the antenna.	11
Figure 2.1	The analyzed photographs of focal lines A, B, C and D respectively as provided by Dr. Mark Halpern. For a clearer photograph of antenna see Figure 1.4	14
Figure 2.2	This figure shows the components of the CHIME structure that are most relevant to this thesis. On the left is a zoomed in section of the a focal line highlighting a joint plate and a cassette respectively. On the right are the corresponding structural drawings from which the dimensions are obtained. Both structures are machined and water jet cut to preset dimensions. . .	15
Figure 2.3	This is a plot of the centroid data in pixel coordinates as seen on the picture for focal line A. The x axis represents the x coordinate on the image in pixels, the y axis represents the y coordinate on the image in pixels. The data plotted is the coordinate position of the line's centers x_i, y_i . The top plot shows the "outer" data set with a linear fit. Similarly, the bottom plot shows the "inner" data set with a linear fit.	17
Figure 2.4	A plot of the cassette's edge deviation from average in pixel coordinates. This is simply Figure 2.3 with the linear fit subtracted out.	18

Figure 2.5	The millimeter per pixel ratio as a function of x coordinate. The x axis is again the x coordinate on the image in pixels, the y axis is the ratio of millimeters to pixels. The data plotted in this figure is the ratio of known separation to measured length l_i . The top plot shows the function for the outer data set (603.6 mm scale) and the bottom plot shows that function for the inner data set (400mm scale)	19
Figure 2.6	A plot of the cassette's edge deviation from average in millimeters. This is Figure 2.4 with the y axis converted into millimeters using the ratios from Figure 2.5	20
Figure 2.7	This is a plot of the final results in the East-West direction. The x axis is the antenna number ranging from 0 to 256 (South to North) and the y axis is the position offset in meters. The colours blue, orange, green and red correspond to focal line A, B, C and D respectively	20
Figure 2.8	This is a plot of the focal line shape as seen in the photographs. The x and y axis represent the pixel coordinates on the photograph. The red points are the positions of the pairs of bolts that are separated by 603.6 mm (corresponding to the outer data set). The black lines are the linear fits used to determine the perspective calculations. This shape is that of a rectangle that has undergone a perspective transformation.	23
Figure 2.9	This is a plot of the millimeter per pixel ratio function f_x . The x axis is the x coordinate in pixels, the y axis is the millimeter per pixel ratio. The data plotted is the ratio between L/N and $x_i + dx_i$ for N = 10,000.	24

- Figure 2.10 This is a plot of the deviation from average separation along the North-South direction of focal line A. The x axis is the x coordinate on the photograph in pixels, the y axis is the deviation from the average North-South separation in millimeters. The separation between two points is calculated by evaluating Equation 2.3, we then follow the same procedure as we did for the East-West direction. Note in this case the presented deviations do not represent deviation from the array position, that is because along the focal line the deviations from average separation would accumulate 25
- Figure 2.11 This is a plot of the deviation from regular a grid along the North-South direction of focal line A. The x axis is the x coordinate on the photograph in pixels, the y axis is the deviation from the average North-South separation in millimeters. The data plotted is found by fixing the positions of the first and last cassette edges and dividing the line into a grid with g_i being the position of point i on the grid. We then plot $g_i - s_i$ where $s_i = \int_{x_0}^{x_i} \Delta x \sqrt{f_x^2(x) + f_y^2(x)(\Delta y/\Delta x)^2}$ 26
- Figure 3.1 An East-West cross section of a CHIME reflector. The orange circle represents a point source $R \ll D$ away from the reflector where $D = 4f$ where f is the focal length. The source radiation encounters the aperture at an angle θ from zenith. The green line represents the path of the wave from the aperture to the antenna represented by a green circle. 28
- Figure 3.2 This figure is the result produced by numerically integrating Equation 3.4 using python. This is a simple model of the complex beam function $A_i(\hat{\mathbf{n}})$ with the real part plotted on top and the phase plotted below. The x axis is θ/π where θ is the angle from the zenith, the y axis are the magnitude and the phase in units of π respectively. 29

Figure 3.3	An East-West cross section of a CHIME reflector similar to Figure 3.1. The red circle represents the positions of the antenna assuming it is shifted by δx . The red line represents the path of a wave detected at the deviated position. ϕ is the angle of the reflection point measured from the focus, it parameterises the reflector as a function of x (position on the aperture). The parameter Δ is the offset in perceived aperture source position for a given reflection point.	31
Figure 3.4	This figure is the result produced by numerically integrating Equation 3.11 using python with $\delta x = 1.5\text{cm}$. The blue plot is the simple beam model as seen in Figure 3.2, the orange plot is the modified beam. It is clear that the position deviation manifests as a pointing offset in the simple beam. The axis are the same as Figure 3.2.	33
Figure 3.5	This is a plot of the offset of the beam's peak as a function of East-West deviation. The main feature of the plot is that the offset increases linearly with deviation. The horizontal "lags" are assumed to be due to the numerical integration and can be corrected for by taking the linear fit through the origin.	34
Figure 3.6	This figure is an identical set up to Figure 3.3 with the deviation along the east-west direction replaced with a deviation δz along the vertical direction.	35
Figure 3.7	This figure is the result produced by numerically integrating Equation 3.16 using python with $\delta z = 1\text{cm}$ (blue) and $\delta z = 10\text{cm}$ (orange). The blue plot is the simple beam model as seen in Figure 3.2. The vertical deviation results in a "flattening" effect on the magnitude, the effect is not observable for small δz	36
Figure A.1	The experimental set up for the mock focal line experiment. Plastic knives are used to mimic the antenna, the meter rule represents the focal line with known dimensions.	44

Glossary

BAO Baryon Acoustic Oscillation

CHIME Canadian Hydrogen Intensity Mapping Experiment

DRAO Dominion Radio Astrophysical Observatory

Acknowledgments

I would like to thank my supervisor Dr. Mark Halpern for teaching me everything I know about the approach to experimental scientific research. I would like to thank Dr. Gary Hinshaw for showing me the beauty of data driven science. Thank you to Tristan Pinsonneault-Marotte for being my primary source of contact on this project and guiding me through all the difficulties that were encountered. I would also like to thank Mateus Fandino for his willingness to answer my questions and discuss my ideas on his own time.

The completion of this project would have not been possible if it was not for the entire UBC CHIME group. Their feedback during the meetings as well as their tips and advice with regards to approaching science in general were of the utmost value.

Finally, thank you to all of my family and friends, who supported me in a variety of ways regardless of their stance on the importance of scientific inquiry and the pursuit of knowledge. Special thanks to my partner Hina Mahboob for being my primary source as well as intellectually challenging me and providing me feedback on my work throughout the last year of my undergraduate.

Chapter 1

Introduction

1.1 Motivation

The most revolutionary discovery in cosmology since Hubble observed that the Universe is expanding is that this expansion is accelerating. A revelation that was awarded the 2011 Nobel Prize for its profound implications. [1]. An accelerating universe implies that either our understanding of gravity is flawed or that a mysterious pressure known as Dark Energy is driving the expansion [15]. This Dark Energy accounts for most (68.3%) of the energy density in the observable universe, however its origin and physics are presently unknown [2]. As a result, the nature of Dark Energy is considered one of the greatest mysteries of modern science [3].

One of the most promising techniques to probe Dark Energy is measuring the baryon acoustic oscillation (BAO), a large scale feature of the matter distribution in the universe left over from the aftermath of the big bang. A novel way to perform this measurement is to use fluctuations in the distribution of the most abundant element in the universe; hydrogen [12].

The Canadian Hydrogen Intensity Mapping Experiment (CHIME) is a large transit radio telescope that aims to constrain the dark energy equation of state by mapping the BAO and providing a history of the expansion of the universe [14, 16]. CHIME is composed of four 100 x 20 m cylindrical reflectors with 1024 dual polarized antenna feeds positioned on the focal lines. CHIME will map out a larger volume of the Universe than has ever been measured by a single astronomical

survey [3]. The telescope is designed to operate in the frequency range 400-800 MHz (redshift $0.8 < z < 2.5$) encompassing the epoch when dark energy began to dominate the energy density of the Universe [14].

CHIME uses a technique known as interferometry in order to observe the sky. CHIME operates under the assumption that the feeds form a regular lattice acting as a large interferometer array. However, in practice it is impossible to achieve a perfectly regular lattice. As a result, there currently exists irregularities in the positions of the feeds. In order to for CHIME to achieve its scientific goal of constraining the dark energy equation of state it must be well calibrated so that the data obtained is of sufficient precision. Antenna feed array irregularities would induce systematic errors in the BAO measurements, and create additional challenges in the foreground removal process while hindering gain calibration and data compression efforts.

In this thesis we use photogrammetry techniques to accurately determine the location of the feeds and thereby measuring deviations from a regular lattice. We then investigate and analyze the basic effects of these irregularities on the instruments performance with an emphasis on data compression efforts and beam effects (using a simple diffraction model of the beam). That will enable us to comment on potential pitfalls of the data capture and compression procedures in order to correct for them.

1.2 Theory & Background

1.2.1 Dark Energy & The Expansion of The Universe

In 1929 Edwin Hubble observed a roughly linear relationship between the redshifts and distances of galaxies, and thus, Hubble's law was discovered [11]. This discovery was the first in a series of evidence for a non static universe. In 1998 observations of Type Ia Supernovae provided evidence that the expansion rate is accelerating, a discovery that revolutionized the field of cosmology [9, 18]. Type Ia Supernova are considered standard candles as their luminosity is well known, this means that one can use the apparent brightness of a supernova in order to measure its distance [8, 9]. The redshift of the supernovae can be found by studying

their light's spectral lines. Adam Reiss et al found that high redshift supernovae are, on average, 10% - 15% farther than one would expect [8, 18]. This deviation from expectation indicates that the rate at which the universe is expanding is accelerating. This acceleration can be accounted for by the reintroduction of a cosmological constant into Einstein's equation [9].

To understand the evolution of a non static universe we turn to the Friedman equations [13]. The Friedman equation describes the conservation of energy in the universe and is given by

$$H^2 = \left(\frac{\dot{a}}{a}\right)^2 = \frac{8\pi G}{3}\rho - \frac{kc^2}{R^2a^2} \quad (1.1)$$

where H is the Hubble parameter, a is the scale factor of the universe, G is the gravitational constant, ρc^2 is the energy density, c is the speed of light, R is the distance between two points in space, and k is a constant related to the curvature of the universe [13]. Observation suggests that the universe is flat and thus, $k = 0$ [20]. We can therefore simplify Equation 1.1 to

$$\dot{a}^2 = \left(\frac{8\pi G}{3}\rho\right)a^2 \quad (1.2)$$

We are now ready to investigate the dynamics of an accelerating universe. We differentiate Equation 1.2 with respect to time and rearrange to get

$$\frac{\ddot{a}}{a} = \frac{4\pi G}{3}(\dot{\rho}\frac{a}{\dot{a}} + 2\rho) \quad (1.3)$$

we then consider the first law of thermodynamics for a dynamic universe with pressure P given by

$$c^2\dot{\rho} + 3\frac{\dot{a}}{a}(c^2\rho + 3P) = 0 \quad (1.4)$$

putting together Equation 1.3 and Equation 1.4 we get

$$\frac{\ddot{a}}{a} = \frac{-4\pi G}{3}(\rho + 3P) \quad (1.5)$$

This result indicates that in order for the expansion of the universe to have a positive acceleration, the universe must have a component with pressure $P < -\rho/3$

[20]. However, a gas of baryonic matter, photons, neutrinos or Weakly Interacting Massive Particles has positive pressure, resulting from the random thermal motions of particles in the gas. For that reason we introduce a cosmological constant that meets this negative pressure requirement [20]. The average density ρ can be separated into the known energy forms

$$\rho = \rho_0 + \frac{\rho_3}{a^3} + \frac{\rho_4}{a^4} \quad (1.6)$$

where $\rho_4 c^2$ is the present value of radiation energy density, $\rho_3 c^2$ is the present value of matter energy density, and $\rho_0 c^2 = \Lambda$ is the cosmological constant representing the energy density of vacuum space (Dark Energy) [9, 13, 20]. This indicates that the universe would progress from radiation dominated state to matter dominated state to a Dark Energy dominated state. We now define a the quantity

$$w = \frac{P}{\rho} \quad (1.7)$$

as a way to describe a variety of universes. For $w = 0$, we have a flat, matter-dominated universe, for $w = 1/3$, we have a radiation dominated universe, for $w = -1$ we have a Dark Energy dominated universe [9]. Measurements from Planck [2] yield $w = -1.006 \pm 0.045$ indicating a Dark Energy dominated universe made up of 68.3% Dark Energy, 26.8% Dark Matter and 4.9% atoms. CHIME aims to measure deviations of w from negative one [4]

1.2.2 Baryon Acoustic Oscillation (BAO)

The standard model of cosmology (the Λ CDM model) assumes that quantum fluctuations in the early universe were pushed to cosmological scales by inflation resulting in Gaussian, adiabatic fluctuations in the distribution of matter [19]. Following inflation the universe consisted of a hot and dense plasma in which baryons and electrons were too energetic to combine, resulting in a charged plasma where photons were constantly interacting with matter via thompson scattering unable to travel far [16]. This interaction results in a radiation pressure acting in the opposite direction of gravity [7]. This pressure prevents gravitational collapse and drives oscillation in the distribution of matter in a manner similar to that of sound

waves in air, i.e. given an over-dense region in the plasma, baryons and photons will propagate outwards in a mechanism similar to that of a spherical sound wave [6, 7]. These oscillations are what is referred to as Baryon Acoustic Oscillations (BAO).

Around 380,000 years after the big bang the universe had cooled to about 3000 K allowing electrons and ions to combine forming neutral hydrogen. At that moment the universe became transparent as photons became free to radiate away unimpeded (the mean free path of photons became larger than the Hubble distance), creating the Cosmic Microwave Background (CMB) and putting an end to the radiation pressure that was driving the BAO. As a result the matter distribution froze with only gravity guiding any subsequent evolution in density [16]. The distance traveled by the sound wave up until this point corresponds to ≈ 150 Mpc comoving [7]. On this scale the expansion of the universe becomes the dominating factor in the evolution of the BAO. This means that BAO provide a length scale that can be used to probe the expansion history of the universe [7, 21]. Since dark energy is the entity responsible for the accelerating expansion of the universe, probing the expansions history is the best cosmological probe for dark energy [21]. Figure 1.1 provides an overview of the timeline of the universe.

As the Universe expanded, the matter distribution acted as seeds for structure formation. This means that by measuring cosmic structure as a function of time, we can deduce the apparent size of the BAO scale as a function of epoch and hence the expansion history of the Universe.

1.2.3 Hydrogen Intensity Mapping

Most of the ordinary matter in the universe is composed of neutral hydrogen, therefore mapping the hydrogen intensity of the universe is a promising method for accurately measuring BAO [4]. Hydrogen intensity mapping allows the apparent angular and radial BAO scale to be measured without needing to resolve individual galaxies [14].

One can map the hydrogen in the universe by looking for 21 cm hyperfine transition emission from neutral hydrogen. This is a transition between the two lowest energy levels in hydrogen arising as a result of spin-spin coupling between the pro-

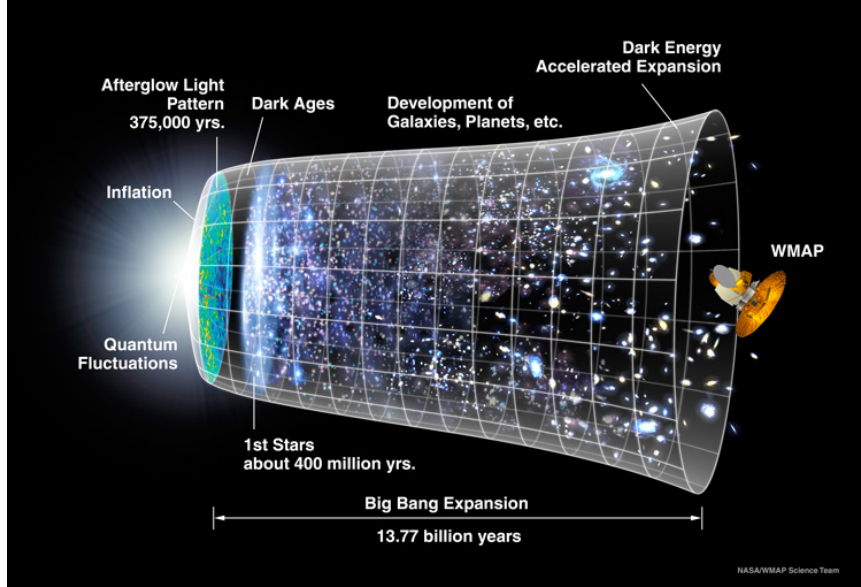


Figure 1.1: A representation of the evolution of the universe over 13.77 billion years. The x axis represents the progression of time, the vertical extent of the grid depicts the size of the universe. The far left depicts the earliest moments when inflation pushed the quantum fluctuations to cosmological scales. The universe then progressed to the dark ages, epoch of reionization and then galaxies and large structures began to form [23]. CHIME aims to probe the region at which the grid size began to curve outwards indicating acceleration due to dark energy dominance.

ton and the electron [10]. The hyperfine energy gap is $5.88 \times 10^{-6} eV$, therefore a photon emitted through this transition has a wavelength of $\approx 21cm$ (hence the name 21cm cosmology) [10]. This wavelength falls in the radio range, which is advantageous for surveys as they can penetrate cosmic clouds and reach us smoothly, additionally it is isolated in the astronomical radio spectrum making it practical for obtaining the redshift of the observed source [17]. The density of the hydrogen intensity is proportional to brightness measurements and thus, allowing us to observe the BAO as overdensities of diffuse hydrogen gas in galaxies along the spherical shell structure of BAO.

1.3 Interferometers

Interferometry is the method of superimposing waves in order to extract information from their interference. The basic interferometer is composed of two antenna whose outputs are correlated. This method in the context of CHIME is best illustrated by studying the simplest example of a radio interferometer, the two-element quasi-monochromatic interferometer. This simple example is of crucial importance as even the most elaborate interferometers (e.g. CHIME) with $N \gg 2$ antennas can be treated as $N(N - 1)/2$ independent interferometer pairs [5]. Therefore, we study this example in detail highlighting its relevance to the project (i.e. the importance of knowing the feed positions with a high accuracy).

Two-Element Quasi-Monochromatic Interferometer (Point Source)

As the name suggests this interferometer uses two antenna feeds to observe a very narrow frequency range centered at $\nu = \omega/(2\pi)$ (see Figure 1.2). Consider a point source stationary in the sky (relative to our reference frame), then the feeds output voltages are time dependant and are represented by $V_i = V \cos(\omega t)$. These voltages are sent to the correlator where they are amplified, multiplied and averaged.

The diagram(Figure 1.2) clearly indicates a difference between the paths traveled by the wave-front to reach the two antenna, the path to feed 1 is $\vec{b} \cdot \hat{s}$ longer than the path to feed 2. Were \vec{b} is the baseline separation vector between the two feeds and \hat{s} is the direction from which the wave-front is approaching. As a result we have an offset in the phase of feed 1 by

$$\tau = \frac{\vec{b} \cdot \hat{s}}{c} \quad (1.8)$$

were c is the speed of light. Therefore, at a given time t the output voltages of the feeds are given by

$$V_1 = V \cos(\omega(t - \tau)) \quad (1.9)$$

$$V_2 = V \cos(\omega(t)) \quad (1.10)$$

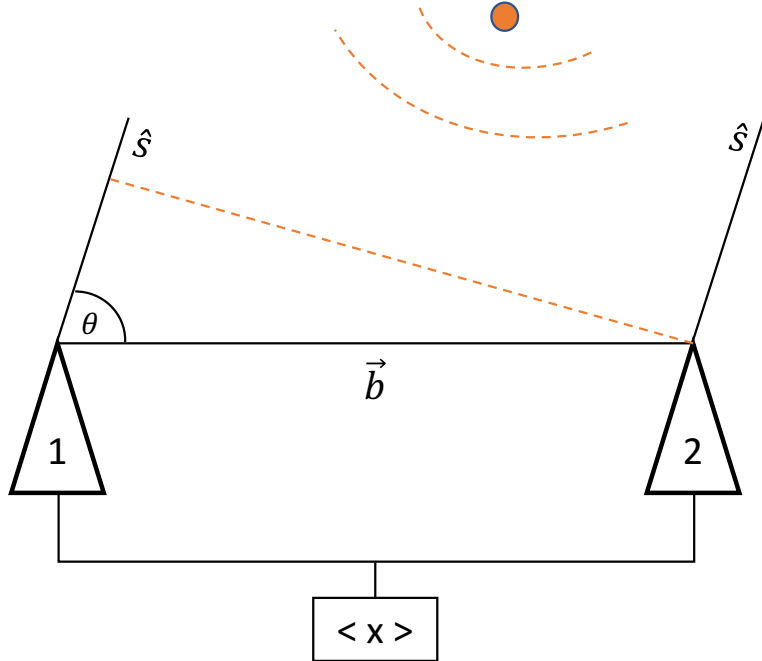


Figure 1.2: This is a diagram of a two-element interferometer. The two triangles labeled 1 and 2 represent two antenna separated by a baseline vector \vec{b} . The straight orange line represents the wavefront coming from a source in the \hat{s} direction, feeds 1 and 2 are receiving the same signal with a phase offset due to the path difference seen in the diagram (the path to feed 1 is $\vec{b} \cdot \hat{s}$ longer than the path to feed 2) The $\langle \times \rangle$ component of the diagram represents the correlator, the component responsible for combining the signal from the two feeds.

these voltages are multiplied in the correlator yielding $V_1 V_2 = V^2 \cos(\omega(t - \tau)) \cos(\omega t) = (V^2/2)(\cos(\omega\tau) + \cos(2\omega t - \omega\tau))$ the correlator then takes a time average long enough to remove the $\cos(2\omega t - \omega\tau)$ term. Leaving us with the final correlator response as

$$R_c = \langle V_1 V_2 \rangle = \left(\frac{V^2}{2} \right) \cos(\omega\tau) \quad (1.11)$$

This example highlights the importance of knowing the value of \vec{b} to a high accuracy, uncertainty in the feed positions would result in calculating a false \hat{s} from a

given output τ , i.e. our telescope is not "pointing" where we think it is.

Two-Element Quasi-Monochromatic Interferometer (Extended Source)

Since in general a source is not limited to behaving as a point source, we briefly generalize the previous calculation to account for extended sources.

The idea is to treat an extended source as a sum of independent point sources, with $I_\nu(\hat{s})$ representing the sky brightness distribution near the frequency ν . Building on the previous calculation we have the correlator response as

$$R_c = \int I_\nu(\hat{s}) \cos(\omega \vec{b} \cdot \hat{s}/c) d\Omega = \int I_\nu(\hat{s}) \cos(2\pi \vec{b} \cdot \hat{s}/\lambda) d\Omega \quad (1.12)$$

where Ω is the solid angle. However, this response is clearly only sensitive to the even component of the brightness distribution, i.e. we need to add in the odd component. This can be done by including a second correlator output with a 90 degree phase delay resulting in

$$R_s = \int I_\nu(\hat{s}) \sin(2\pi \vec{b} \cdot \hat{s}/\lambda) d\Omega \quad (1.13)$$

We now combine the two responses to achieve the desired result. We define the visibility $\mathcal{V} = R_c + iR_s$ giving us the final response to an extended source as

$$\mathcal{V} = \int I_\nu(\hat{s}) e^{-i2\pi \frac{\vec{b} \cdot \hat{s}}{\lambda}} d\Omega \quad (1.14)$$

Again we note the explicit dependence on \vec{b} highlighting the importance of knowing the value to a high accuracy. For completeness we also point out that this result can be further generalized for a finite frequency range. This can be done by integrating over ν in the desired range prior to integrating over Ω .

Far-Field Approximation

It is clear that the above calculations rely on the underlying assumption that the incident wave is planar. In this subsection we perform a quick calculation to verify that this assumption is justified. Consider the set up in Figure 1.3, by Pythagoras

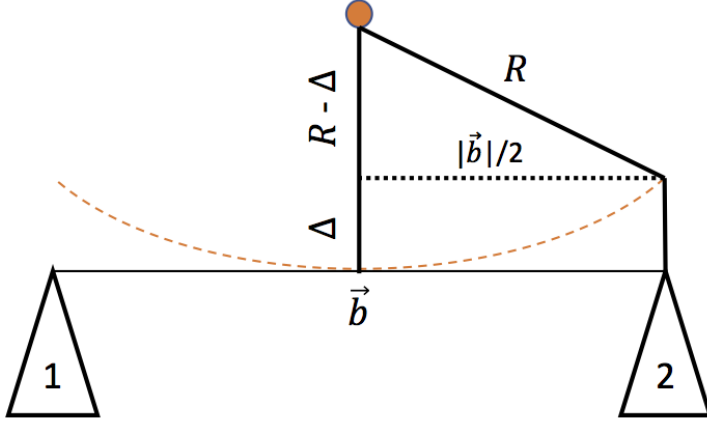


Figure 1.3: This diagram shows the same interferometer as Figure 1.2, the orange line represents the spherical wave front upon arrival at the feeds. The parameter Δ parameterizes the deviation from a planar wave and R represents the distance between the wave and the source.

theorem we have

$$R^2 = (R - \Delta)^2 + \left(\frac{|\vec{b}|}{2}\right)^2 \quad R = \frac{\Delta}{2} + \frac{|\vec{b}|^2}{8\Delta} \quad (1.15)$$

therefore in the limit $\Delta \ll |\vec{b}|$, we have $\Delta/2 \ll |\vec{b}|^2/(8\Delta)$ and as a result

$$R \approx \frac{|\vec{b}|^2}{8\Delta} \quad (1.16)$$

It is clear that as R goes to infinity Δ goes to 0, i.e. for sources far away we can treat an incoming spherical wave as planar. In practice we require the source to be at a distance such that $\Delta \ll \lambda$, a somewhat arbitrary convention is to require $\Delta < \lambda/16$ therefore requiring the source to be further than $2|\vec{b}|^2/\lambda$. For CHIME that distance is on the order of 5km, meaning our approximation holds for astronomical sources.



Figure 1.4: Photographs of CHIME: The top photograph shows the CHIME telescope from a distance, the four cylindrical reflectors are the large white structures oriented along the north-south direction. At the focal line of each reflector is 256 antenna mounted below a walkway. The bottom photograph shows one of the focal line walkways, the green devices seen in the photograph are the antenna.

1.4 An Introduction to CHIME

CHIME is a transit radio interferometer telescope located at the Dominion Radio Astrophysical Observatory (DRAO) in Penticton, BC. The telescope is designed to operate in the frequency range 400-800 MHz (redshift $0.8 < z < 2.5$) encompassing the era during which the Λ CDM model predicts dark energy began to dominate the energy density of the Universe. CHIME has no moving parts, it utilizes the planet's rotation to survey half of the sky each sidereal day providing us with sufficient

Reflector Dimensions	100 m × 20 m
Number of Feeds	256 per reflector (1024)
Frequency Range	400 - 800 MHz
Frequency Resolution	0.39 MHz
Wavelength range	75 - 37 cm
Redshift range	$0.8 < z < 2.5$
Epoch	11 - 8 Gyr
Field of View	N-S: 90°, E-W: 2.5° – 1.3°

Table 1.1: Summary of CHIME instrument salient features

volume to measure the BAO comoving scale [3, 9].

The instrument consists of four adjacent cylindrical reflectors oriented along the north-south direction, each cylinder is 100m by 20m with a 5m focal length f (See Figure 1.4). This geometry results in a field of view of 90° along the North-South direction and 1.3° – 2.5° in the East-West [14]. Over each reflector is a walkway with 256 dual polarized antenna mounted below along the reflector’s focal line (See Figure 1.4). Electromagnetic radiation from the sky is focused by the reflectors onto the antenna, the resulting signals are then amplified and guided to a receiver hut at which they undergo second stage amplification and digitization. The digitized signals are then channelized into 1024 frequency bins of range 0.39 MHz and correlated. Table 1.1 provides a summary of instrument features discussed and as seen in [14].

Chapter 2

Antenna Feed Deviation Measurements

The focus of this chapter is to use a set of photographs of the CHIME focal lines Figure 2.1 (one photograph per focal line) in order to extract the deviations in the position of the antenna along the East-West and North-South directions. The four pictures are similar enough to be analyzed using the same general procedure, however the pictures are not identical and therefore there are minor differences between focal lines. The general methodology will be presented in the context of one of the focal lines (focal line A) with the results presented for each focal line separately.

2.1 General Method

The general approach used in extracting the antenna deviations revolves around taking advantage of the our knowledge of CHIME's structure and dimensions. Each set of four antenna are mounted onto the focal line via a metallic structure we refer to as a cassette Figure 2.2. The cassettes are bolted together using another metallic structure referred to as the joint plate Figure 2.2. The dimensions of both structures are known with high accuracy.

The first step in the general method is to note that for each joint plate in the pictures there are four visible bolts. That is for 256 antenna there are 65-66 vis-

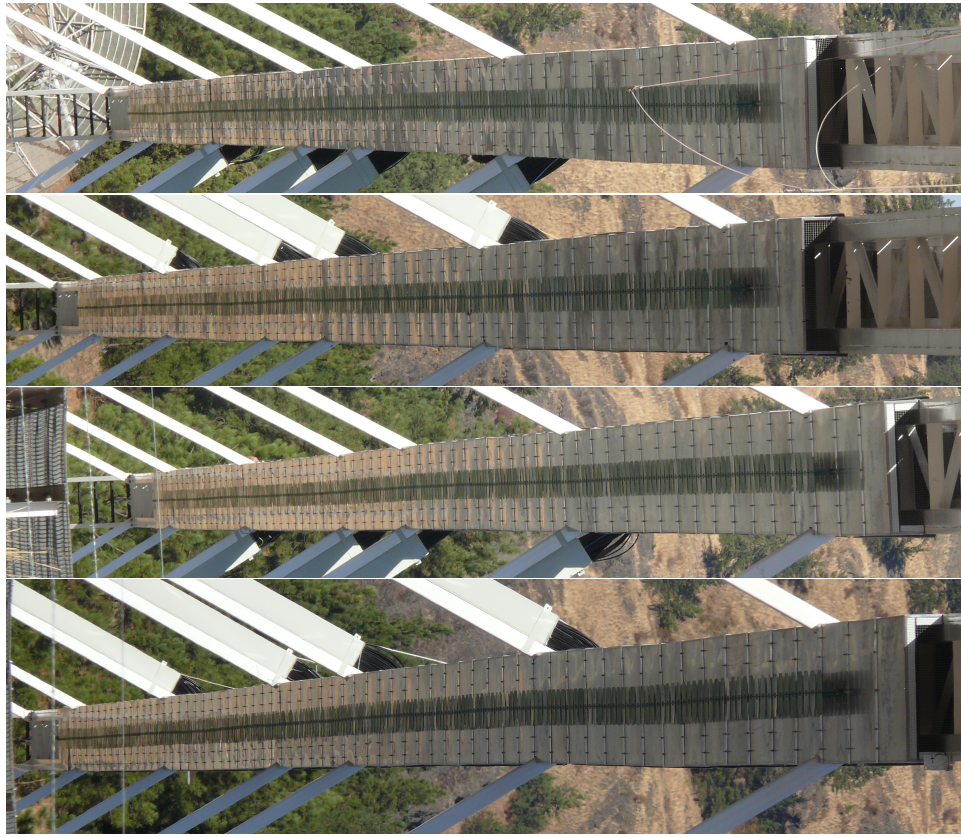


Figure 2.1: The analyzed photographs of focal lines A, B, C and D respectively as provided by Dr. Mark Halpern. For a clearer photograph of antenna see Figure 1.4

ible joint plates corresponding to 64 cassettes. A JAVA based image processing software called imageJ is used to collect two sets of data. The first set (outer) is collected by drawing lines connecting the two bolts furthest apart on the joint plates (with known separation of 603.6 mm), the software records the length of the line, the angle of the line with respect to the horizontal axis and the pixel coordinate of the line's center. The second set (inner) is collected by repeating the process using the pair of bolts with the smallest separation (with known separation of 400 mm). Additional data sets were collected as a means to gauge my consistency and record apparent uncertainty.

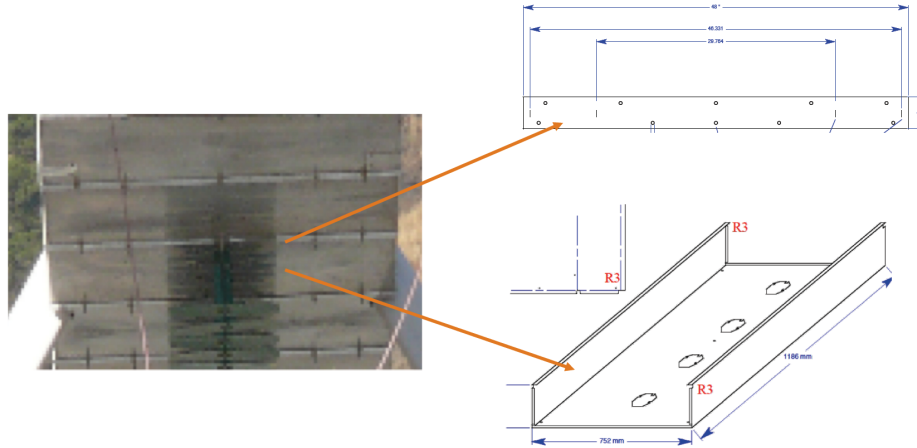


Figure 2.2: This figure shows the components of the CHIME structure that are most relevant to this thesis. On the left is a zoomed in section of the a focal line highlighting a joint plate and a cassette respectively. On the right are the corresponding structural drawings from which the dimensions are obtained. Both structures are machined and water jet cut to preset dimensions.

The second step is to interpret the data. The pixel coordinates recorded correspond to the center of the cassettes' edges. We then determine the average positions of the centers along the two axis of concern and assume that deviation from the average corresponds to deviation from the regular lattice in pixels. We then use the known dimensions of the joint plates in order to determine a millimeter per pixel scale and convert the cassette deviations into millimeters.

The final step is to determine the deviations of the individual antenna feeds. We assume that the cassettes are rigid, this assumption allows us to use the deviations of the cassette edges in order to linearly interpolate the deviations of the individual antenna.

2.2 East-West Deviation

We now present an implementation of this general method by working through the process of extracting the antenna's East-West position offsets for focal line A. The

first step is to import the raw data from imageJ into python. We import the outer and inner data sets in the form $(x_i, y_i, l_i, \theta_i)$ were x_i, y_i are the coordinates in pixels of the center of line i and l_i, θ_i are the line's length and angle respectively. After the data is imported we plot the centroid data in pixel coordinates and produce a linear fit as seen in Figure 2.3. As one would expect, the data is distributed in a random but continuous manner around the average linear fit. One feature that might seem interesting in Figure 2.3 is the fact that the recorded uncertainty increases at large x . The reason for this is the image perspective effects. At large x the focal line is closer to the camera resulting in higher resolution image of the bolts, meaning each bolt occupies more pixels than for smaller x values. Uncertainty in bolt position varies between 1 and 2 pixels depending on the location on image.

We are now ready to extract the East-West deviation of the cassettes. This is done by simply subtracting out the average from the centroid data the resulting deviations are plotted in Figure 2.4. Before we can extract the antenna position offsets from the cassette's deviations we must convert our data into millimeters. This can be done by using the known separations of the bolts. The photographs in Figure 2.1 indicate that to a good approximation the depth perception varies only as a function of x . This means that the millimeter per pixel ratio is independent of y and thus will not vary along l_i . Therefore, we can convert the deviation of point i into millimeters by multiplying it with $603.6/l_i$ for the outer data set and $400/l_i$ for the inner data set. The ratio as a function of x is presented in Figure 2.5. Figure 2.6

Now that we have the cassette edge deviations we can determine the offset of each antenna feed. Assuming the cassettes are rigid and that within each cassette the antenna are equally separated, we can determine the antenna offsets via linear interpolation. This procedure is repeated for the remaining focal lines. The final results are presented in Figure 2.7. One feature to note is that for focal lines C and D the last four antenna are taken to be at the same deviation, that is because in the corresponding images only one cassette edge was visible for the final cassette and therefore the interpolation was not possible.

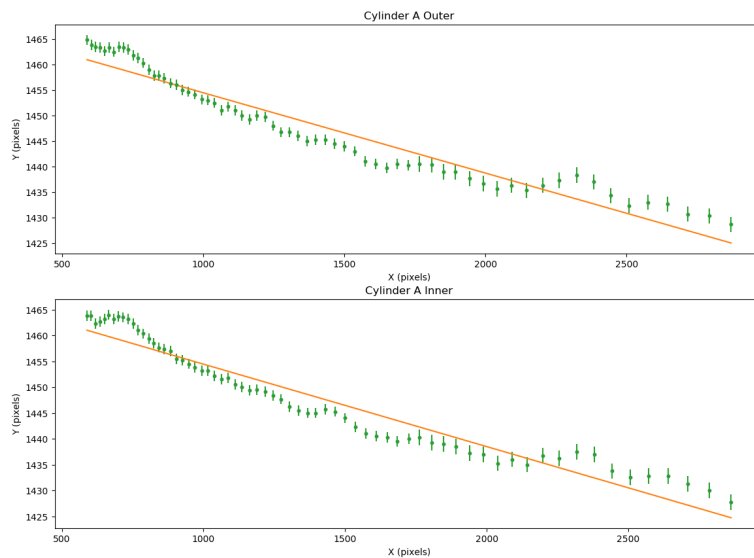


Figure 2.3: This is a plot of the centroid data in pixel coordinates as seen on the picture for focal line A. The x axis represents the x coordinate on the image in pixels, the y axis represents the y coordinate on the image in pixels. The data plotted is the coordinate position of the line's centers x_i, y_i . The top plot shows the "outer" data set with a linear fit. Similarly, the bottom plot shows the "inner" data set with a linear fit.

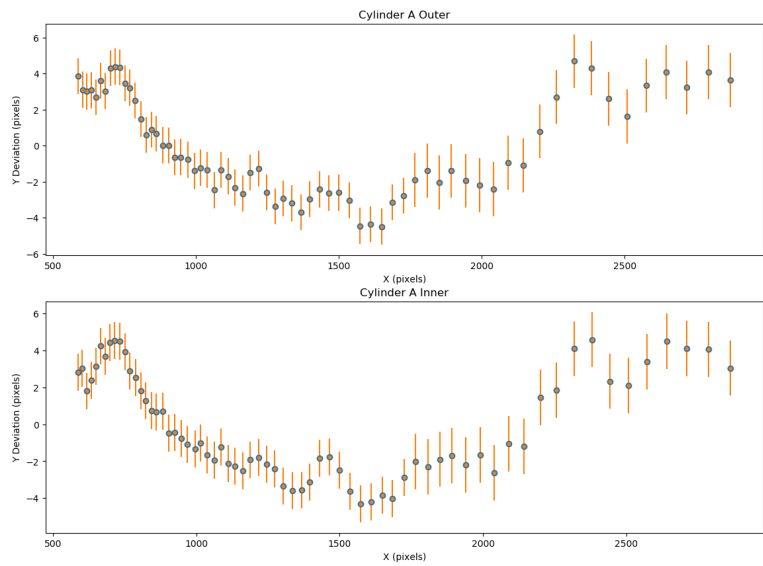


Figure 2.4: A plot of the cassette's edge deviation from average in pixel coordinates. This is simply Figure 2.3 with the linear fit subtracted out.

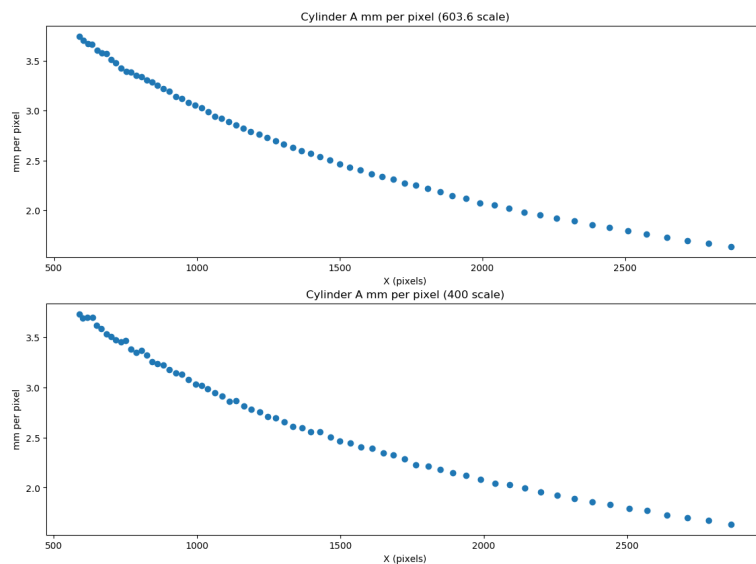


Figure 2.5: The millimeter per pixel ratio as a function of x coordinate. The x axis is again the x coordinate on the image in pixels, the y axis is the ratio of millimeters to pixels. The data plotted in this figure is the ratio of known separation to measured length l_i . The top plot shows the function for the outer data set (603.6 mm scale) and the bottom plot shows that function for the inner data set (400mm scale)

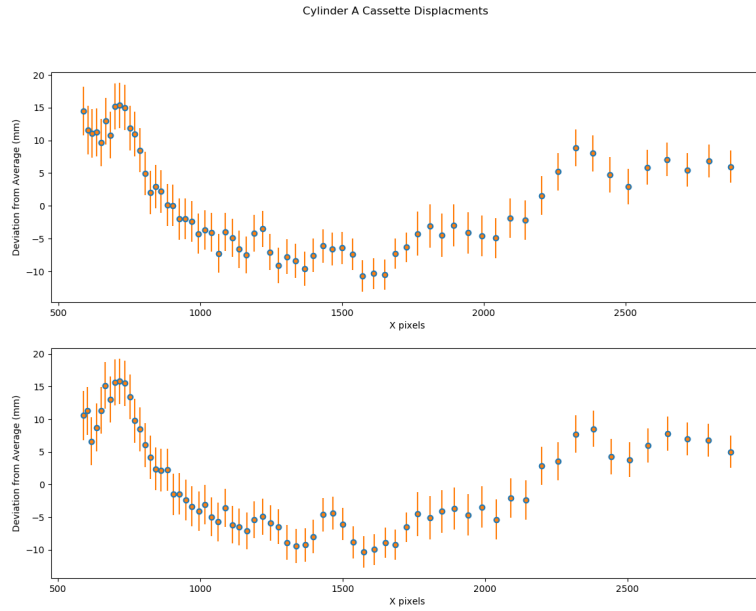


Figure 2.6: A plot of the cassette's edge deviation from average in millimeters. This is Figure 2.4 with the y axis converted into millimeters using the ratios from Figure 2.5

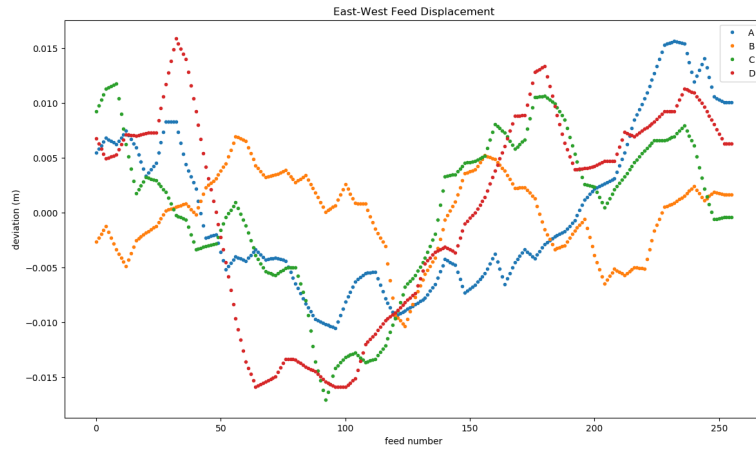


Figure 2.7: This is a plot of the final results in the East-West direction. The x axis is the antenna number ranging from 0 to 256 (South to North) and the y axis is the position offset in meters. The colours blue, orange, green and red correspond to focal line A, B, C and D respectively

2.3 North-South Deviation

We now turn to the extraction of the North-South deviations. This task is significantly more complex as the millimeter per pixel ratio continuously varies along the x direction. As a result the cassette edge separations cannot be determined via a simple subtraction of coordinates. In order solve this problem we must account for the perspective effects in our calculations, this can be done by introducing the following discrete metric

$$(\Delta s)^2 = f_x^2(x, y)(\Delta x)^2 + f_y^2(x, y)(\Delta y)^2 \quad (2.1)$$

where Δs is the distance on the focal line in millimeters, $\Delta x, \Delta y$ are the components of the distance in pixel coordinates and f_x, f_y are the functions providing the millimeter per pixel ratio. If we confine our analysis to the focal line, we can use the same assumption as in the previous section, depth varies only as a function of x. Therefore, f_x, f_y are independent of y and we can rewrite Equation 2.1 as

$$(\Delta s)^2 \approx f_x^2(x)(\Delta x)^2 + f_y^2(x)(\Delta y)^2 \quad (2.2)$$

This assumption is valid to a good approximation as the depth variation along the y direction is at the 2% rate, which is of lower significance than the Shaaban induced human error. This means that if we can determine f_x and f_y we can measure the separation between two points on the photographs by taking the following integral

$$s = \int_{x_i}^{x_{i+1}} \Delta x \sqrt{f_x^2(x) + f_y^2(x)(\Delta y/\Delta x)^2} \quad (2.3)$$

In order to find f_x and f_y let us consider the special case $\Delta x \ll \Delta y$, this implies that

$$\Delta s \approx f_y(x)\Delta y \quad (2.4)$$

Both of our data sets happen to satisfy that condition, this is because the line connecting two bolts in the photographs is almost perfectly perpendicular to the x axis. This means that we already have enough information to determine the

function f_y . We have the value of the function at x_i for all i given by

$$f_y(x_i) = \frac{\Delta s}{l_i \sin \theta_i} \approx \frac{\Delta s}{l_i} \quad (2.5)$$

this is the same data presented in Figure 2.5. We can obtain the function by numerically fitting a polynomial model to the data. Now the only piece of information left is f_x . To find this function we will proceed as follows, we use our $(x_i, y_i, l_i, \theta_i)$ data in order to retrieve the pixel coordinates of the tagged bolts and fit a linear line through them to determine the general shape of the focal line. This result is presented in Figure 2.8, as one might expect the shape is that of a rectangle that has undergone a perspective transformation. Perspective transformations map straight lines to straight lines, therefore, we can find the center point of that shape by drawing two diagonal lines connecting the top right corner to the bottom left corner and the top left corner to the bottom right corner. The intersection point of the two lines will correspond to the center point of the shape. This process can be recursively repeated dividing the shape into N slices of equal length L/N where L is the known total length of the rectangle in millimeters. We take N large enough such that f_x is assumed to be constant over the slice. We can then find f by using

$$f_x(x_i) = \frac{L}{N \Delta x_i} \quad (2.6)$$

The result is a millimeter per pixel function presented in Figure 2.9. At this point we are ready to calculate the deviations, however we first note the following issue. As previously discussed the uncertainty will range from 1-2 pixels in the y direction. Along the x direction the uncertainty is even greater as we would have to account for perspective effects. If we assume the best case scenario and take 1-2 pixel uncertainty along the x direction this indicates that our uncertainty in deviation will range from 40 mm to 160 mm. This is problematic since the span of the cassettes was measured using survey equipment and the length found deviates from the expected span by only a few millimeters. Additionally the cassettes are bolted in place so it is unrealistic to expect them to move around in the order of centimeters. Thus, we have to assume that the deviation for the cassette edges would be on the order of a few millimeters therefore rendering our data of no use as it provides us with no new information due to the large uncertainty. Nonetheless,

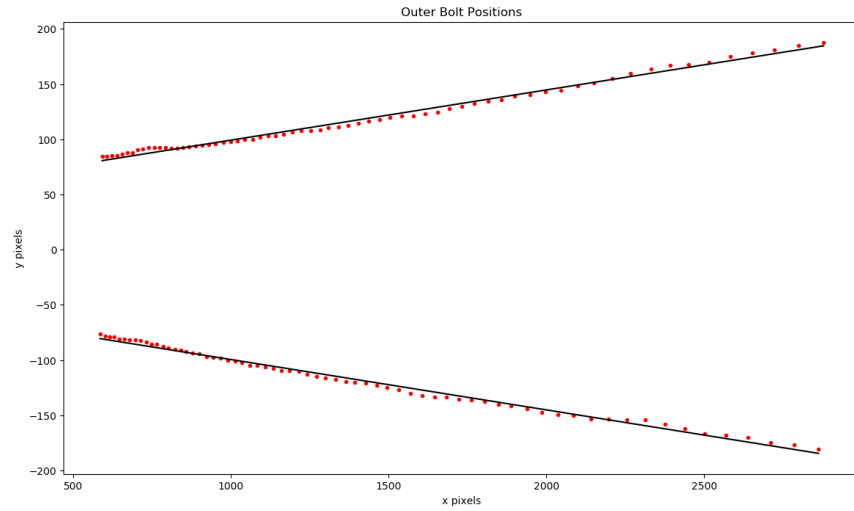


Figure 2.8: This is a plot of the focal line shape as seen in the photographs.

The x and y axis represent the pixel coordinates on the photograph. The red points are the positions of the pairs of bolts that are separated by 603.6 mm (corresponding to the outer data set). The black lines are the linear fits used to determine the perspective calculations. This shape is that of a rectangle that has undergone a perspective transformation.

for the sake of completion we find the deviation along the North-South direction and present the results in Figure 2.10 and Figure 2.11.

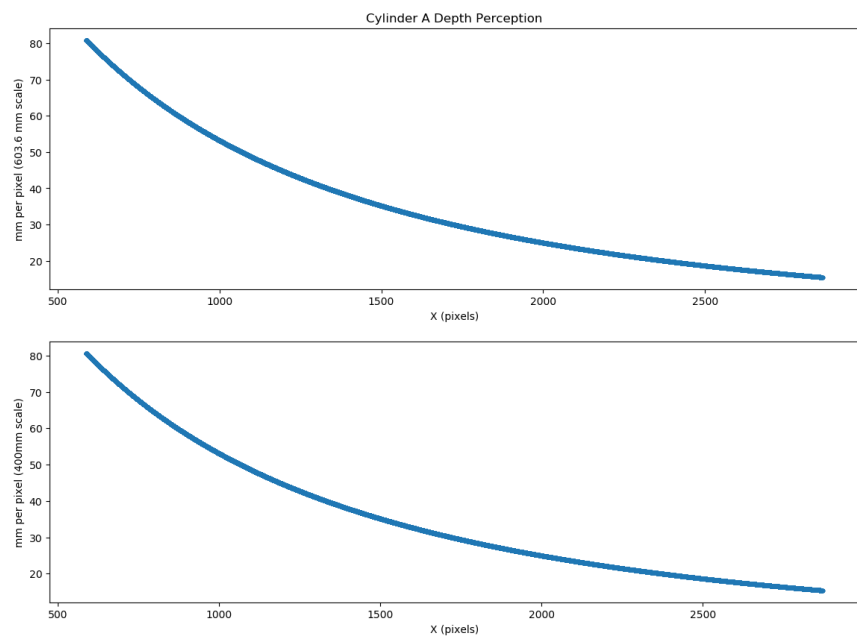


Figure 2.9: This is a plot of the millimeter per pixel ratio function f_x . The x axis is the x coordinate in pixels, the y axis is the millimeter per pixel ratio. The data plotted is the ratio between L/N and $x_i + dx_i$ for N = 10,000.

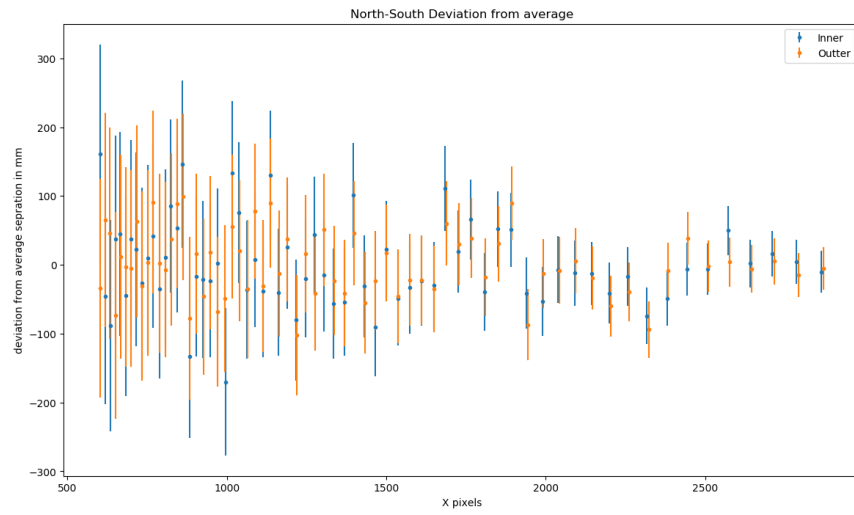


Figure 2.10: This is a plot of the deviation from average separation along the North-South direction of focal line A. The x axis is the x coordinate on the photograph in pixels, the y axis is the deviation from the average North-South separation in millimeters. The separation between two points is calculated by evaluating Equation 2.3, we then follow the same procedure as we did for the East-West direction. Note in this case the presented deviations do not represent deviation from the array position, that is because along the focal line the deviations from average separation would accumulate

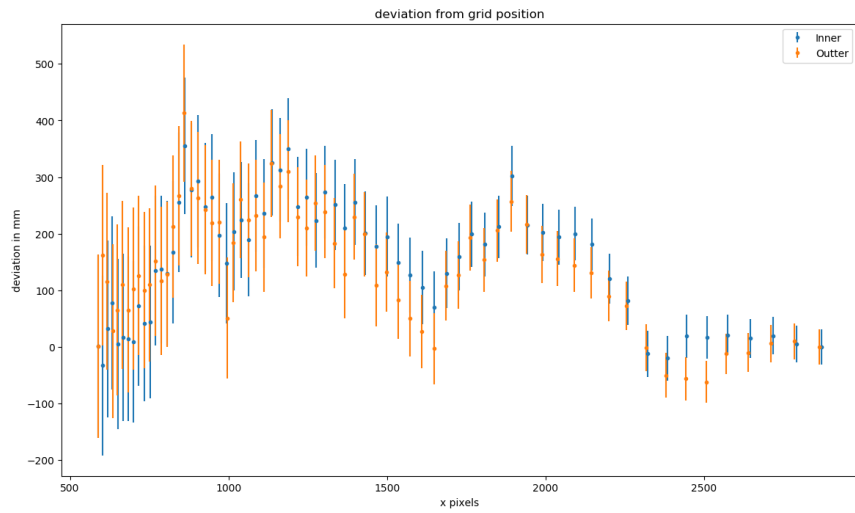


Figure 2.11: This is a plot of the deviation from regular a grid along the North-South direction of focal line A. The x axis is the x coordinate on the photograph in pixels, the y axis is the deviation from the average North-South separation in millimeters. The data plotted is found by fixing the positions of the first and last cassette edges and dividing the line into a grid with g_i being the position of point i on the grid. We then plot $g_i - s_i$ where $s_i = \int_{x_0}^{x_i} \Delta x \sqrt{f_x^2(x) + f_y^2(x)(\Delta y/\Delta x)^2}$.

Chapter 3

Feed Deviation Effects

3.1 Deviation Effects on A Simple Beam Model

The instantaneous CHIME visibility expressed with the notation used in [22] is given by

$$V_{ij} \propto \int d^2\hat{\mathbf{n}} A_i(\hat{\mathbf{n}}) A_j^*(\hat{\mathbf{n}}) e^{2\pi i \hat{\mathbf{n}} \cdot \mathbf{u}_{ij}} T(\hat{\mathbf{n}}) \quad (3.1)$$

where u_{ij} is the baseline separation between two feeds in units of wavelength, $\hat{\mathbf{n}}$ is the position in the celestial sphere, $A_i(\hat{\mathbf{n}})$ is the primary beam of feed i and $T(\hat{\mathbf{n}})$ is the brightness temperature of the sky at $\hat{\mathbf{n}}$.

In this chapter we will investigate the effects of changing \mathbf{u}_{ij} to $\mathbf{u}_{ij} + \Delta\mathbf{u}_{ij}$. The CHIME beam is fairly complicated as it needs to account for a variety of different factors, as a result for this investigation we will be assuming a simple beam model described in Section 3.1.1.

3.1.1 Simple Beam Model

For our calculations we will be looking at a simple beam model derived from the diffraction pattern of the electric field at the focal point. For this model we assume a perfectly smooth surface of the reflector and ignore any beam bounce. Additionally, we assume that the antenna response is constant as a function of angle.

Considered a plane wave encountering a cross-section of the parabolic reflector

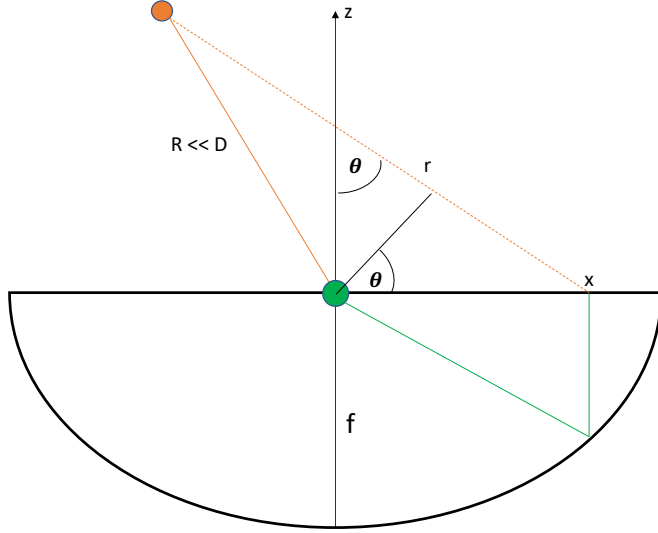


Figure 3.1: An East-West cross section of a CHIME reflector. The orange circle represents a point source $R \ll D$ away from the reflector where $D = 4f$ where f is the focal length. The source radiation encounters the aperture at an angle θ from zenith. The green line represents the path of the wave from the aperture to the antenna represented by a green circle.

at angle θ from zenith with the source located $R \ll D$ away from the focus. For CHIME $D = 4f$ where f is the focal length (see Figure 3.1). We set our origin at the focus so that our aperture spans $x \in [-2f, 2f]$. We then let $r(x)$ be the distance from the source to an element of the aperture extending from x to $x + dx$. By the Fraunhofer approximation we can express this distance using Equation 3.2 [5]

$$r(x) \approx R + x \sin(\theta) \quad (3.2)$$

To calculate the interference of the electric field at the focus as a function of θ we can treat the aperture as a continuous array of sources, phased as to reproduce the incoming plane wave. Therefore the field radiated from each element is given by Equation 3.3

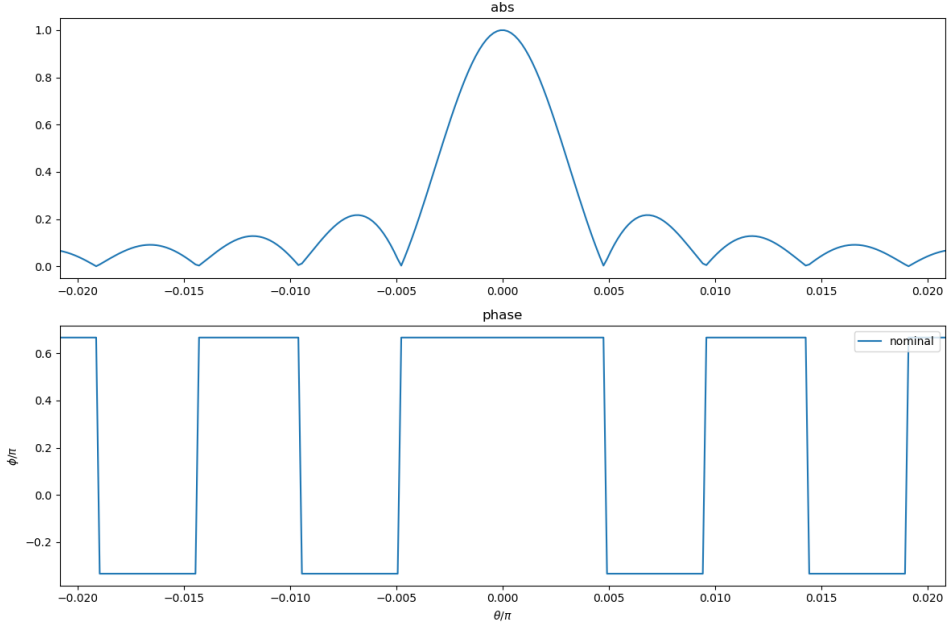


Figure 3.2: This figure is the result produced by numerically integrating Equation 3.4 using python. This is a simple model of the complex beam function $A_i(\hat{\mathbf{n}})$ with the real part plotted on top and the phase plotted below. The x axis is θ/π where θ is the angle from the zenith, the y axis are the magnitude and the phase in units of π respectively.

$$dE \propto e^{-2\pi i x \sin \theta / \lambda} \quad (3.3)$$

and thus, we obtain the electric field by simply integrating over the aperture

$$E(\theta) \propto e^{2\pi i 2f/\lambda} \int_{-2f}^{2f} e^{-2\pi i x \sin \theta / \lambda} dx \quad (3.4)$$

were a factor of $e^{2\pi i 2f/\lambda}$ is added to account for the distance traveled from the aperture to the focus. Numerically integrating Equation 3.4 results in the familiar sinc pattern seen in Figure 3.2. For the remainder of this document we will assume this pattern to be the unperturbed form of $A_i(\hat{\mathbf{n}})$ for all feeds i .

3.1.2 Visibility Phase Effects

We are now ready to begin considering the effects of the position deviations on the instrument. For the remainder of this chapter the deviation in position of an antenna will be represented by $\delta x_i \hat{x} + \delta y_i \hat{y} + \delta z_i \hat{z}$ were $\hat{x}, \hat{y}, \hat{z}$ correspond to East-West, North-South and vertical directions respectively. We will begin our investigation by ignoring the beams and focusing on the visibility phase factor $e^{2\pi i \hat{n} \cdot \mathbf{u}_{ij}}$. In order to account for the deviations we change $\hat{\mathbf{n}} \cdot \mathbf{u}_{ij}$ to $\hat{\mathbf{n}} \cdot (\mathbf{u}_{ij} + \Delta \mathbf{u}_{ij})$ were $\Delta \mathbf{u}_{ij} = (\delta x_i + \delta x_j) \hat{x} + (\delta y_i + \delta y_j) \hat{y} + (\delta z_i + \delta z_j) \hat{z}$. As a result, our CHIME visibilities (Equation 3.1) will change as follows

$$V_{ij} \rightarrow V_{ij} e^{\hat{\mathbf{n}} \cdot \Delta \mathbf{u}_{ij}} \quad (3.5)$$

3.1.3 Visibility Beam Effects

We now turn to the beam functions $A_i(\hat{\mathbf{n}})$ and investigate how they are impacted by the deviations. We begin by considering the case of deviation in the antenna position along the north-south direction. This is the simplest case to handle as a position offset along the focal line would not change the cross section used in Figure 3.1. As a result, our simple beam functions $A_i(\hat{\mathbf{n}})$ are unaffected. Thus, deviation along the north-south direction will manifest solely as the change in phase discussed in Section 3.1.2. We will now proceed by investigating the effect of the East-West and vertical deviations on the beam.

East-West Deviation Beam Effects

Unlike deviation in the North-South direction, East-West deviations cannot be solely expressed as phase effects. To see why we turn to Figure 3.3. We now use the same procedure used to derive the simple beam model with modifications introduced based on the geometry of the problem. To simplify the problem we must first shift our thinking, rather than integrating over the aperture elements we integrate over the reflection points, i.e. over the surface of the reflector, using $\phi(x) \in [-\pi/2, \pi/2]$ were ϕ is the angle from the focus. We now note that each reflection point will no longer correspond to the same aperture element as in the original problem, the element is shifted by Δ as seen in Figure 3.3 as a result of

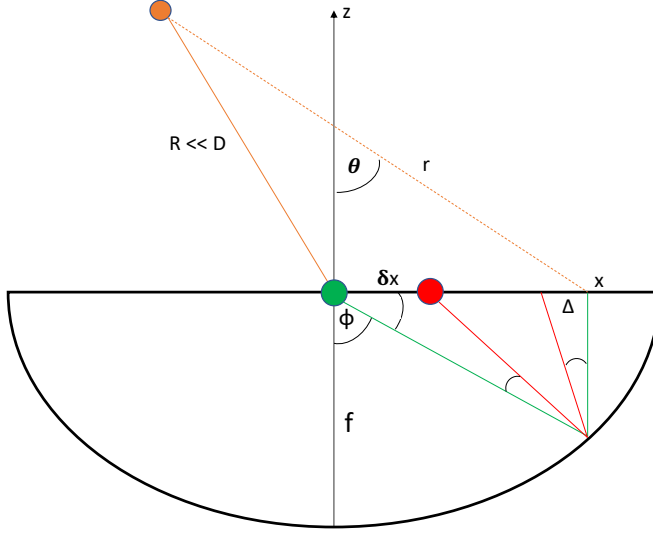


Figure 3.3: An East-West cross section of a CHIME reflector similar to Figure 3.1. The red circle represents the positions of the antenna assuming it is shifted by δx . The red line represents the path of a wave detected at the deviated position. ϕ is the angle of the reflection point measured from the focus, it parameterises the reflector as a function of x (position on the aperture). The parameter Δ is the offset in perceived aperture source position for a given reflection point.

the δx offset of the antenna. Therefore, we must adjust Equation 3.3 accordingly by changing x to $x - \Delta$. We also note that the path traveled by the wave from the aperture to the antenna is no longer a constant but varies as a function of x so we must also appropriately change $2f$ to $l(x)$. Modifying Equation 3.3 to account for the geometry gives us

$$dE \propto e^{-2\pi i(x-\Delta)\sin\theta/\lambda} e^{2\pi i l(x)/\lambda} \quad (3.6)$$

The next step is to determine the quantities Δ and $l(x)$ as a function of x . We begin by dividing the path traveled by the wave from the aperture to the antenna into two paths, the path from the aperture source to the reflector p_s and the path

from the reflector to the antenna p_a such that $p_s + p_a = 2f$. We then use similar angles to derive the following expression

$$\Delta = \frac{p_s}{p_r - \delta x \sin \phi} \delta x \cos \phi \quad (3.7)$$

this expression can be rewritten as $\Delta = \delta x \cos \phi (\frac{p_s}{p_r} + \frac{p_s}{p_r^2} \delta x \sin \phi + \dots)$. Keeping only terms to first order in δx and noting that $p_s/p_r = \cos \phi$ we are left with the following clean expression

$$\Delta \approx \delta x \cos^2 \phi \quad (3.8)$$

The next step is to get the new path length by using Pythagoras theorem

$$l(x) = \sqrt{\Delta^2 + p_s^2} + \sqrt{(\delta x \cos \phi)^2 + (p_r - \delta x \sin \phi)^2} \quad (3.9)$$

expanding the square roots keeping only terms to first order in δx simplifies the result to

$$l(x) \approx 2f - \delta x \sin \phi \quad (3.10)$$

We are now ready to get our modified beam functions. Integrating Equation 3.6 gives the expression

$$E(\theta) \propto e^{2\pi i 2f/\lambda} \int_{-\pi/2}^{\pi/2} e^{-2\pi i (x - \delta x \cos^2 \phi) \sin \theta / \lambda} e^{-2\pi i \delta x \sin \phi / \lambda} d\phi \quad (3.11)$$

this expression is then numerically integrated using python resulting in Figure 3.4. The first order effect of the deviation on our simple beam manifests as a pointing offset and thus replacing $A_i(\hat{\mathbf{n}})$ with $A_i(\hat{\mathbf{n}} - \delta \hat{\mathbf{n}})$. Finally we study the relationship between the offset and the size of δx and present it in Figure 3.5

Vertical Deviation Beam Effects

We now consider deviation along the vertical axis as depicted in Figure 3.6. Using the same approach and notation as Section 3.1.3 we consider the geometry of the figure to find Δ and $l(x)$ and use Equation 3.6 to determine find the field. We use

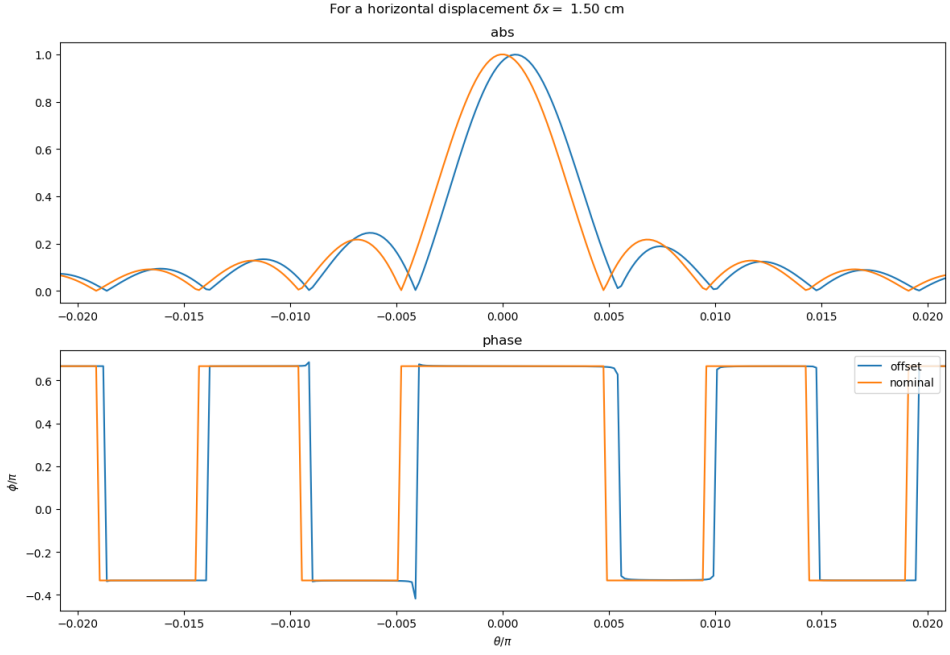


Figure 3.4: This figure is the result produced by numerically integrating Equation 3.11 using python with $\delta x = 1.5\text{cm}$. The blue plot is the simple beam model as seen in Figure 3.2, the orange plot is the modified beam. It is clear that the position deviation manifests as a pointing offset in the simple beam. The axis are the same as Figure 3.2.

similar angles to derive the following expression

$$\Delta = \frac{p_s}{p_r - \delta z \cos \phi} \delta z \sin \phi \quad (3.12)$$

this expression can be rewritten as $\Delta = \delta z \sin \phi \left(\frac{p_s}{p_r} + \frac{p_s}{p_r^2} \delta z \cos \phi + \dots \right)$. Keeping only terms to first order in δz and noting that $p_s/p_r = \cos \phi$ we are left with the following clean expression

$$\Delta \approx \delta z \cos \phi \sin \phi \quad (3.13)$$

The next step is to get the new path length by using Pythagoras theorem

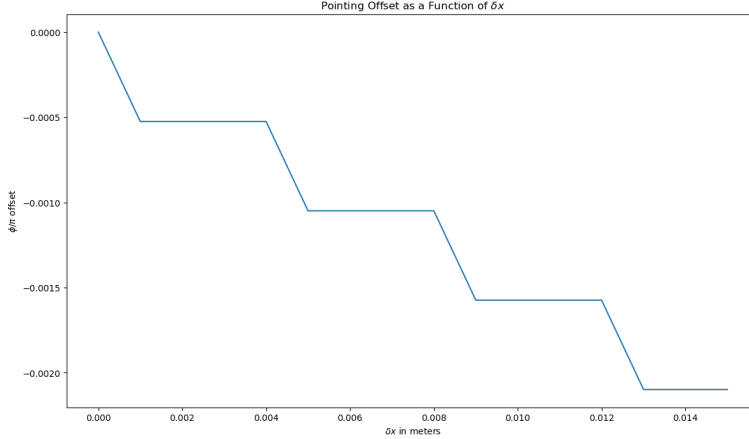


Figure 3.5: This is a plot of the offset of the beam's peak as a function of East-West deviation. The main feature of the plot is that the offset increases linearly with deviation. The horizontal "lags" are assumed to be due to the numerical integration and can be corrected for by taking the linear fit through the origin.

$$l(x) = \sqrt{\Delta^2 + p_s^2} + \sqrt{(\delta z \sin \phi)^2 + (p_r - \delta z \cos \phi)^2} \quad (3.14)$$

expanding the square roots keeping only terms to first order in δx simplifies the result to

$$l(x) \approx 2f - \delta x \sin \phi \quad (3.15)$$

We are now ready to get our modified beam functions. Integrating Equation 3.6 gives the expression

$$E(\theta) \propto e^{2\pi i 2f/\lambda} \int_{-\phi_{max}}^{\phi_{max}} e^{-2\pi i (x - \delta x \cos \phi \sin \phi) \sin \theta / \lambda} e^{-2\pi i \delta x \cos \phi / \lambda} d\phi \quad (3.16)$$

The bounds of the integral are determined by the angle at which the reflection off the surface can no longer reach the feed. This expression is then numerically integrated using python resulting in Figure 3.7. The deviation manifests in a complicated manner changing $A_i(\hat{\mathbf{n}})$ to $A'_i(\hat{\mathbf{n}})$.

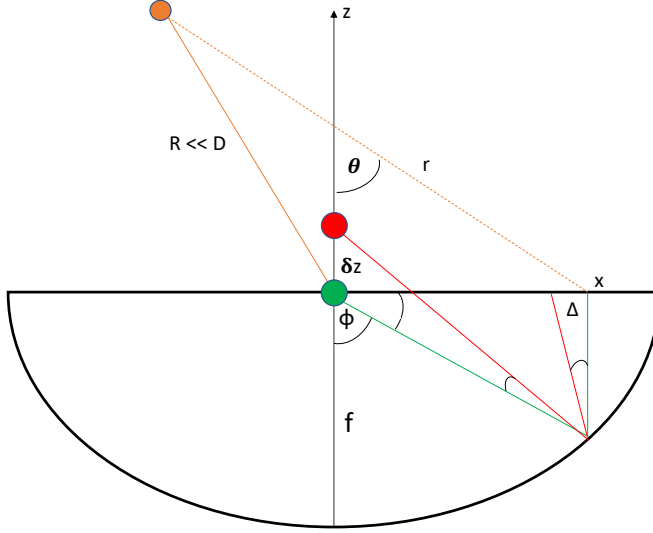


Figure 3.6: This figure is an identical set up to Figure 3.3 with the deviation along the east-west direction replaced with a deviation δ_z along the vertical direction.

We can now include the measured effects into the CHIME data by modifying the visibility appropriately. The modified visibility is

$$V_{ij} \propto \int d^2\hat{\mathbf{n}} A'_i(\hat{\mathbf{n}} - \delta\hat{\mathbf{n}}_i) A'^*_j(\hat{\mathbf{n}} - \delta\hat{\mathbf{n}}_j) e^{2\pi i \hat{\mathbf{n}} \cdot \mathbf{u}_{ij}} e^{\hat{\mathbf{n}} \cdot \Delta \mathbf{u}_{ij}} T(\hat{\mathbf{n}}) \quad (3.17)$$

3.2 Deviation Effects on Redundant Baseline Stacking

Unfortunately due to the additional time spent on researching a valid strategy to extract the North-South deviations I was unable to complete this analysis in time for the submission of this thesis. Current progress on this topic includes a comparison of the singular value decomposition of a "true" redundant visibility matrix and the same decomposition with variations along the East-West direction introduced. No results of sufficient quality for this thesis are ready at this moment.

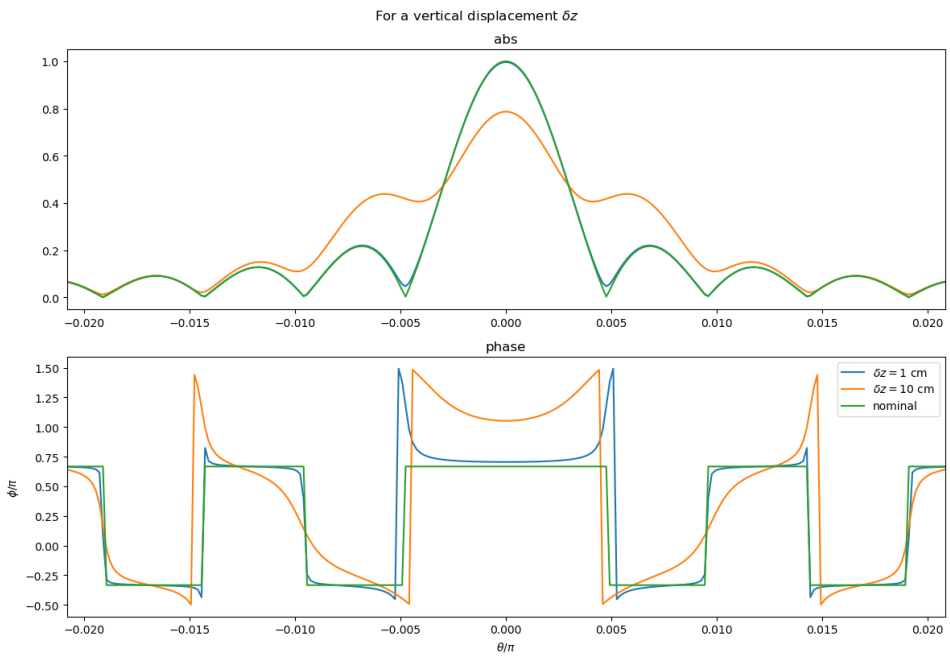


Figure 3.7: This figure is the result produced by numerically integrating Equation 3.16 using python with $\delta z = 1\text{cm}$ (blue) and $\delta z = 10\text{cm}$ (orange). The blue plot is the simple beam model as seen in Figure 3.2. The vertical deviation results in a "flattening" effect on the magnitude, the effect is not observable for small δz .

Chapter 4

Discussion & Future Work

4.1 Future Work

The analysis presented in this thesis indicates that further work needs to be conducted with regards to analyzing the antenna feed positions and their impact on the instrument. This future work can be divided into two categories. The first, a more complete investigation on the impact of the measured deviations on the instrument. The second, gather more data in order to extract the North-South and Vertical direction deviations.

With regards to further analyzing the data extracted in this thesis several avenues need to be explored. We have already begun analyzing the impact of the deviations on redundant baseline stacking, therefore, a natural place to start future work on this topic would be to complete this analysis. Deviations along the East-West direction could potentially play a non trivial role resulting in data loss during the redundant stacking procedures. This data can also be easily combined with existing code to produce a synthesized beam that accounts for the deviations, comparing this with the expected synthesized beam would provide further insight into the deviation effects and is therefore another avenue that should be explored moving forward.

The analysis conducted in Chapter 3 should be done using more sophisticated beam models, while this task might be complicated the results presented in the chapter can be utilized with the help of perturbation theory to simplify the

problem. Finally, a complicated but important future task would be to simulate sky maps with the deviations accounted for and compare the result with the non deviated sky maps.

In addition further analyzing the data extracted in this thesis, more data should be obtained. As previously discussed, we were unable to extract useful North-South deviation data using the photographs analyzed in this thesis. New data can be acquired by simply taking more photographs of the focal line from a variety of different known locations. By doing so vertical deviations can be obtained by comparing pictures taken from different angles while North-South deviations can be obtained in the same manner used in this thesis.

4.2 Conclusion

The investigation tackled in this thesis has provided us with useful antenna position data as well as identified some of the effects of such deviations on the instrument. Our photo analysis has produced high accuracy measurements of how much each antenna feed deviates from its expected position along the East-West direction. The results indicate that for all four cylinders the deviation is bounded by 1.5 cm.

We developed some useful techniques and methods to extract the deviations of the antenna along the North-South direction, however our data accuracy was limited due to the resolutions of the photographs analyzed. The uncertainty in our data along the North-South direction is too large for the measurements to be of much use in the impact analysis.

By assuming a simple beam model using the diffraction pattern at the focus we analyzed the impact of the position offsets on the visibility matrix. North-South deviations manifest exclusively as a phase off-set and can therefore be easily accounted for. East-West deviations manifest to first order as a pointing offset making them more complicated to handle. Finally, vertical deviations perturb the shape of the beam. However, for deviation within 2 cm the perturbed beam is almost indistinguishable from its unperturbed counterpart, as a result, if the vertical deviations are measured to be within the expected range of bound by 1cm then the deviation effect can be considered to be exclusively a phase to a good approximation.

Bibliography

- [1] The nobel prize in physics 2011 - advanced information. nobelprize.org., 2014. → pages 1
- [2] P. A. R. Ade et al. Planck 2013 results. I. Overview of products and scientific results. *Astron. Astrophys.*, 571:A1, 2014.
doi:10.1051/0004-6361/201321529. → pages 1, 4
- [3] K. Bandura, G. E. Addison, M. Amiri, J. R. Bond, D. Campbell-Wilson, L. Connor, J.-F. Cliche, G. Davis, M. Deng, N. Denman, M. Dobbs, M. Fandino, K. Gibbs, A. Gilbert, M. Halpern, D. Hanna, A. D. Hincks, G. Hinshaw, C. Höfer, P. Klages, T. L. Landecker, K. Masui, J. Mena Parra, L. B. Newburgh, U.-l. Pen, J. B. Peterson, A. Recnik, J. R. Shaw, K. Sigurdson, M. Sitwell, G. Smecher, R. Smegal, K. Vanderlinde, and D. Wiebe. Canadian Hydrogen Intensity Mapping Experiment (CHIME) pathfinder. In *Ground-based and Airborne Telescopes V*, volume 9145, page 914522, July 2014. doi:10.1117/12.2054950. → pages 1, 2, 12
- [4] T.-C. Chang, U.-L. Pen, J. B. Peterson, and P. McDonald. Baryon Acoustic Oscillation Intensity Mapping as a Test of Dark Energy. *Phys. Rev. Lett.*, 100:091303, 2008. doi:10.1103/PhysRevLett.100.091303. → pages 4, 5
- [5] J. J. Condon and S. M. Ransom. Essential radio astronomy. National Radio Astronomy Observatory, 2010. URL <http://www.cv.nrao.edu/course/astr534/ERA.shtml>. → pages 7, 28
- [6] D. J. Eisenstein. Measuring cosmic distances with the baryon acoustic oscillations. University of Chicago Lecture, 2008. → pages 5
- [7] D. J. Eisenstein et al. Detection of the Baryon Acoustic Peak in the Large-Scale Correlation Function of SDSS Luminous Red Galaxies. *Astrophys. J.*, 633:560–574, 2005. doi:10.1086/466512. → pages 4, 5

- [8] A. V. Filippenko, A. G. Riess, and High-Z Supernova Search Team. Evidence from Type Ia supernovae for an accelerating universe. In J. F. Nieves, editor, *Particle Physics and Cosmology*, volume 540 of *American Institute of Physics Conference Series*, pages 227–246, Oct. 2000. doi:10.1063/1.1328887. → pages 2, 3
- [9] D. C. Good. *Redundant baseline calibration in CHIME: a first implementation application as beam probe*. PhD thesis, University of British Columbia, 2017. URL <https://open.library.ubc.ca/cIRcle/collections/24/items/1.0355206>. → pages 2, 3, 4, 12
- [10] D. Griffiths. *Introduction to Quantum Mechanics*. Cambridge University Press, 2016. ISBN 9781107179868. URL <https://books.google.ca/books?id=0h-nDAAAQBAJ>. → pages 6
- [11] E. Hubble. A relation between distance and radial velocity among extra-galactic nebulae. *Proceedings of the National Academy of Sciences*, 15(3):168–173, 1929. ISSN 0027-8424. doi:10.1073/pnas.15.3.168. URL <http://www.pnas.org/content/15/3/168>. → pages 2
- [12] A. Loeb and S. Wyithe. Precise Measurement of the Cosmological Power Spectrum With a Dedicated 21cm Survey After Reionization. *Phys. Rev. Lett.*, 100:161301, 2008. doi:10.1103/PhysRevLett.100.161301. → pages 1
- [13] R. J. Nemiroff and B. Patla. Adventures in Friedmann cosmology: A detailed expansion of the cosmological Friedmann equations. *American Journal of Physics*, 76:265–276, Mar. 2008. doi:10.1119/1.2830536. → pages 3, 4
- [14] L. B. Newburgh et al. Calibrating CHIME, A New Radio Interferometer to Probe Dark Energy. *Proc. SPIE Int. Soc. Opt. Eng.*, 9145:4V, 2014. doi:10.1117/12.2056962. → pages 1, 2, 5, 12
- [15] P. J. E. Peebles and B. Ratra. The Cosmological constant and dark energy. *Rev. Mod. Phys.*, 75:559–606, 2003. doi:10.1103/RevModPhys.75.559. → pages 1
- [16] J. B. Peterson, R. Aleksan, R. Ansari, K. Bandura, D. Bond, J. Bunton, K. Carlson, T.-C. Chang, F. DeJongh, M. Dobbs, S. Dodelson, H. Darhmaoui, N. Gnedin, M. Halpern, C. Hogan, J.-M. Le Goff, T. T. Liu, A. Legrouri, A. Loeb, K. Loudiyi, C. Magneville, J. Marriner, D. P. McGinnis, B. McWilliams, M. Moniez, N. Palanque-Delabruille, R. J.

Pasquinelli, U.-L. Pen, J. Rich, V. Scarpine, H.-J. Seo, K. Sigurdson, U. Seljak, A. Stebbins, J. H. Steffen, C. Stoughton, P. T. Timbie, A. Vallinotto, and C. Teche. 21-cm Intensity Mapping. In *astro2010: The Astronomy and Astrophysics Decadal Survey*, volume 2010 of *ArXiv Astrophysics e-prints*, 2009. → pages 1, 4, 5

- [17] J. R. Pritchard and A. Loeb. 21cm cosmology in the 21st century. *Reports on Progress in Physics*, 75(8):086901, 2012. URL <http://stacks.iop.org/0034-4885/75/i=8/a=086901>. → pages 6
- [18] A. G. Riess, A. V. Filippenko, P. Challis, A. Clocchiatti, A. Diercks, P. M. Garnavich, R. L. Gilliland, C. J. Hogan, S. Jha, R. P. Kirshner, B. Leibundgut, M. M. Phillips, D. Reiss, B. P. Schmidt, R. A. Schommer, R. C. Smith, J. Spyromilio, C. Stubbs, N. B. Suntzeff, and J. Tonry. Observational evidence from supernovae for an accelerating universe and a cosmological constant. *The Astronomical Journal*, 116(3):1009, 1998. URL <http://stacks.iop.org/1538-3881/116/i=3/a=1009>. → pages 2, 3
- [19] A. Riotto. Particle cosmology. *ArXiv e-prints*, Oct. 2010. → pages 4
- [20] B. Ryden. *Introduction to Cosmology*. Cambridge University Press, 2016. ISBN 9781107154834. URL <https://books.google.ca/books?id=07WSDQAAQBAJ>. → pages 3, 4
- [21] H.-J. Seo and D. J. Eisenstein. Probing Dark Energy with Baryonic Acoustic Oscillations from Future Large Galaxy Redshift Surveys. , 598:720–740, Dec. 2003. doi:10.1086/379122. → pages 5
- [22] J. R. Shaw, K. Sigurdson, U.-L. Pen, A. Stebbins, and M. Sitwell. All-sky Interferometry with Spherical Harmonic Transit Telescopes. , 781:57, Feb. 2014. doi:10.1088/0004-637X/781/2/57. → pages 27
- [23] N. S. Team. Timeline of the universe. NASA website, 2010. URL <https://map.gsfc.nasa.gov/media/060915/index.html>. → pages vi, 6

Appendix A

Appendix A

The project presented in this thesis is fairly different from the original intended project. I spent a little over a quarter of the time on the original project and will use this section to discuss the work done.

My colleagues and I flew a drone over the CHIME reflectors and captured a large number of photographs of each focal line. The original project intended to use those photographs along with 3D modelling software in order to produce a 3D model of the CHIME focal lines. The 3D models would then be used to extract the antenna feed positions with high accuracy.

I dedicated a week to finding photogrammetry software that is compatible with our goals. I researched the available photogrammetry software found at (https://en.wikipedia.org/wiki/Comparison_of_photogrammetry_software) and choose Agisoft PhotoScan based on its features, user friendliness, export capabilities and cost. A document summarizing my research was put together and presented to my supervisors.

After the software was chosen a mock experiment was set up in order to simultaneously familiarize myself with the software and assess its accuracy. The mock experiment involved putting together a fake focal line using a meter rule and plastic knives (see Figure A.1 and ??). Agisoft Photoscan was used to stitch a total of 100 photographs of the set up and produce a 3D model. The model is not presented in this thesis as downloading it and/or using it would require purchasing the software.

The first indication that this original plan would need to be modified came as a

result of the mock experiment. It was extremely difficult to produce the 3D model as it required a large amount of time consuming manual stitching and the capture of additional photographs. The main and final reason to why the project was altered is the fact that most of the drone captured photographs were out of focus. This occupied the first 2 months of the 7 months long project.



Figure A.1: The experimental set up for the mock focal line experiment. Plastic knives are used to mimic the antenna, the meter rule represents the focal line with known dimensions.